

pubs.acs.org/JCTC Article

Hierarchical Equations of Motion in Matrix Product States: Formalism and Applications for Charge Transport

Hengrui Yang, Zirui Sheng, Liqi Zhou, and Zhigang Shuai*



Cite This: J. Chem. Theory Comput. 2025, 21, 10108-10119



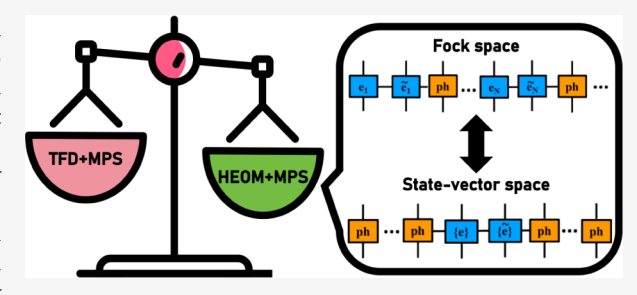
ACCESS

III Metrics & More

Article Recommendations

Supporting Information

ABSTRACT: We present a Hierarchical Equations of Motion (HEOM) approach in the Matrix Product State (MPS) formalism to simulate carrier transport in molecular aggregates described by an electron—phonon Hamiltonian with bosonic dissipation. Transport properties are evaluated through time-dependent population analysis and mobility calculations. The method's validity is rigorously established through benchmarking against conventional HEOM. Comparative analysis with Thermo-Field Dynamics combined with MPS (TFD + MPS) reveals fundamental similarities and differences in their effective Hamiltonians and demonstrates the specific accuracy.



and computational efficiency of our HEOM + MPS framework. For single-electron systems, we introduce state-vector space configurations that enhance performance beyond traditional Fock space approaches. Results confirm that our method provides a robust, nearly exact, and efficient numerical quantum dynamic approach for carrier transport in dissipative bosonic environments.

1. INTRODUCTION

Transport properties present central issues for molecular functional materials, ^{1–3} such as organic solar cells, ^{2,3} optoelectronic materials, ^{4,5} and molecular electronics/devices. ^{6–10} Carrier transport involves electron scattering and relaxation processes within the vibrational environment. While band-like pictures ^{11–13} describe charge transport under weak electron–phonon coupling, most organic semiconductors exhibit significant electron–phonon coupling ^{14–19} due to the flexible backbone structure of organic molecules. ²⁰ Crucially, electron–phonon coupling constitutes a common problem that poses substantial challenges.

A number of numerical methods have been developed to address such problems, including mean-field Ehrenfest dynamics 18,21 and surface hopping, 22,23 which treat nuclear motion classically. Quantum nuclear effects were first predicted theoretically²⁴⁻²⁶ and later confirmed experimentally through nonlinear current-voltage characteristics and isotope effects.²⁷⁻³⁰ While time-dependent density matrix renormalization group³¹⁻³⁶ and multilayer multiconfiguration timedependent Hartree^{37,38} methods can incorporate quantum nuclear effects in electron dynamics, they face limitations and struggle with discretized environmental modes in large systems,³⁹ and both methods encounter numerical challenges from orbital ordering problems.^{33,35,39–45} Theoretical approaches like nonequilibrium Green's function and master equation methods mainly rely on perturbation theory for many-body effects. These collective limitations underscore the need for a more robust computational technique capable of simultaneously handling environments and many-body interactions.

Quantum dynamics for open quantum systems, where bath degrees of freedom are traced, provide an effective framework for addressing the problems. To accurately model carrier transport dynamics, non-Markovian memory effects must be incorporated, necessitating approaches beyond Lindblad equations ^{39,49–52} and Redfield equations. ^{53,54} Several methods based on the reduced density matrix have been developed to capture non-Markovian dynamics in carrier transport, including the pseudo mode method, 55,56 the quasi-adiabatic path integral, 57,58 and hierarchical equations of motion (HEOM). 59-64 If based on the tensor network state ansatz, 65,66 which was first proposed by Shi et al.,63 rather than density matrices or auxiliary density operators (ADOs), the computational cost can be significantly reduced. Notably, tensor network state formalisms have been successfully integrated with diverse open quantum system methodologies, 55,63,67-71 including the matrix product state (MPS) formalism.

Building on our previous development of GPU-accelerated algorithms⁷² and the general autoconstruction method⁷³ for matrix product operators (MPO), we implement HEOM within an MPS formalism using twin space to model charge transport in molecular aggregates with dissipative bosonic

Received: August 19, 2025 Revised: October 6, 2025 Accepted: October 8, 2025 Published: October 16, 2025





environments. For single-electron systems, we develop state-vector space MPS configurations that surpass conventional Fock space approaches in both accuracy and efficiency. We further benchmark our HEOM + MPS framework against Thermo-Field Dynamics combined with MPS (TFD + MPS). 33,42,74–76 Although both methods employ density matrices at finite temperature under initially disentangled system-bath conditions, they originate from fundamentally different effective Hamiltonians and theoretical frameworks: TFD + MPS relies on the discretization of the full quantum space, while HEOM + MPS is based on open quantum dynamics.

2. THEORETICAL MODEL AND METHODOLOGICAL APPROACH

2.1. HEOM for Different Model Hamiltonians. We consider model Hamiltonians partitioned into system, bath, and system—bath coupling components:

$$H = H_{\rm S} + H_{\rm R} + V = H_{\rm 0} + V \tag{1}$$

The system—bath interaction assumes a sum-of-products form: $V = \sum_i S_i B_i$, where $\{S\}$ and $\{B\}$ denote the system and collective bath operators, respectively. The collective bath operators can also be decomposed:

$$B_i = \sum_j g_{ij} q_j \tag{2}$$

with g_{ij} representing the coupling strength and q_j the normal mode coordinate. We assume the initial conditions at t=0 such that baths remain thermally equilibrated at temperature T, obey Gaussian statistical properties, 59,64 and are disentangled from the system. The bath's effect on system dynamics is encoded in bosonic correlation functions:

$$C^{\text{Bose}}(t) = \text{Tr}\{\hat{B}(t)\hat{B}\rho_{\text{B}}\}\$$

$$= \frac{1}{\pi} \int_{-\infty}^{\infty} e^{-i\omega t} J(\omega) f^{\text{Bose}}(\omega) d\omega$$

$$= \sum_{k} \eta_{k} e^{-\gamma_{k} t}$$

$$f^{\text{Bose}} = \frac{1}{1 - e^{-\beta \omega}}$$
(3)

where J is the spectral density function and $f^{\rm Bose}$ is the partition function for the Bose–Einstein distribution. Using Padé or Matsubara decomposition (see Section S1), we expand the bath correlation function as an exponential series, with k being the index of expansion terms. Applying a series of auxiliary influence functionals and their time derivatives can yield the HEOM equation. 59,61,64

The spin-boson model represents the simplest yet most widely adopted benchmark for quantum dynamics. 62,68,69,77 Its Hamiltonian components (eq 1) are explicitly:

$$H_{\rm S} = \varepsilon \sigma_{\!\! z} + \Delta \sigma_{\!\! x}$$

$$H_{\rm B} = \sum_{k} \left(\frac{p_{k}^{2}}{2} + \frac{1}{2} \omega_{k}^{2} q_{k}^{2} \right) = \sum_{k} \omega_{k} \left(b_{k}^{+} b_{k} + \frac{1}{2} \right)$$

$$V = \sigma_{z} \sum_{k} c_{k} q_{k} = \sigma_{z} \sum_{k} \frac{c_{k}}{\sqrt{2\omega_{k}}} (b_{k}^{+} + b_{k})$$
(4)

where σ 's denote Pauli matrices, ε is the energy gap between the two states and Δ is the coupling. w_k , p_k , q_k are the frequency, momentum, and coordinate of the kth mode, respectively. c_k represents the coupling strength and can be described by the following spectral density function, with b_k^+ , b_k the phonon creation and annihilation operators. We employ the Debye–Drude spectral density function, with λ being the reorganization energy and ω_c the cutoff frequency.

$$J(\omega) = \frac{\pi}{2} \sum_{k} \frac{c_k^2}{\omega_k} \delta(\omega - \omega_k)$$
 (5)

$$J(\omega) = \frac{\lambda \omega \omega_{\rm c}}{\omega_{\rm c}^2 + \omega^2} \tag{6}$$

The corresponding HEOM equation 61,62,64 is

$$\dot{\rho}_{n} = -\left(iL_{S} + \sum_{k} n_{k} \gamma_{k}\right) \rho_{n} - i\left[\sigma_{z}, \sum_{k} \rho_{n_{k}^{+}}\right]$$

$$-i\sum_{k} n_{k} (\eta_{k} \sigma_{z} \rho_{n_{k}^{-}} - \eta_{k}^{*} \rho_{n_{k}^{-}} \sigma_{z})$$

$$(7)$$

Here, η_k , γ_k correspond to eq 3 parameters, L_S is the Liouville superoperator $L_S \rho = [H_S, \rho]$, and ρ_n are the so-called auxiliary density operators (ADOs). The multi-index $n = \{n_1, n_2, \cdots, n_k, \cdots\}$ with non-negative integer elements tracks the hierarchy depth, while n_k^{\pm} is an abbreviation for $n \pm 1_k$ with $1_k = \{0, 0, \cdots, 0, 1_k, 0, \cdots\}$, and n_k is the kth element of k. The other details are given in Section 2.3.

The Fenna–Matthews–Olson (FMO) complex has attracted significant interest as a key photosynthetic component.⁷⁸ Its quantum dynamics are described by a Frenkel–Holstein Hamiltonian with exciton–phonon coupling:

$$H_{S} = \sum_{ij}^{N} J_{ij} a_{i}^{+} a_{j}$$

$$H_{B} = \sum_{i=1}^{N} \sum_{k} \omega_{k} b_{ik}^{+} b_{ik}$$

$$V = \sum_{i=1}^{N} \sum_{k} g_{k} \omega_{k} (b_{ik}^{+} + b_{ik}) a_{i}^{+} a_{i}$$
(8)

where a_i^+ (a_i) is the creation (annihilation) operator for the ith local excited state, J_{ij} denotes the excitation energy (i = j) or Coulomb coupling ($i \neq j$), b_{ik}^+ and b_{ik} are phonon creation and annihilation operators of the kth mode with frequency ω_k and electron—phonon coupling

$$g_k = \frac{c_k}{\sqrt{2\omega_k^3}}$$

Using the Debye-Drude spectral density (eq 7), the corresponding HEOM equation is

$$\dot{\rho}_{n} = -\left(iL_{S} + \sum_{i}^{N} \sum_{k} n_{ik} \gamma_{ik}\right) \rho_{n} - i \sum_{i}^{N} \left[a_{i}^{+} a_{i}, \sum_{k} \rho_{n_{ik}^{+}}\right] - i \sum_{k}^{N} \sum_{k} n_{ik} (\eta_{k} a_{i}^{+} a_{i} \rho_{n_{ik}^{-}} - \eta_{k}^{*} \rho_{n_{ik}^{-}} a_{i}^{+} a_{i})$$
(9)

This extends eq 8, with an additional index *i* meaning the exciton site and σ_z replaced by $a_i^+a_i$.

A distinct application is the Peierls model, featuring intermolecular vibrational coupling:

$$H_{S} = \sum_{i} \varepsilon_{i} a_{i}^{+} a_{i} + J \sum_{i} (a_{i}^{+} a_{i+1} + a_{i+1}^{+} a_{i})$$

$$H_{B} = \sum_{i} \sum_{k} \omega_{k} b_{ik}^{+} b_{ik}$$

$$V_{Peierls} = \sum_{i} \sum_{k} g_{k} \omega_{k} (b_{ik}^{+} + b_{ik}) (a_{i}^{+} a_{i+1} + a_{i+1}^{+} a_{i})$$
(10)

considering only the nearest-neighbor couplings. The HEOM equation follows eq 10 except with $a_i^+a_i$ replaced by $a_i^+a_{i+1}+a_{i+1}^+a_i$.

2.2. HEOM in Twin Space. Equations 7 and 9 demonstrate that the HEOM formalism is inherently non-perturbative and non-Markovian. While only the zeroth-tier reduced density operator $\rho_0(t)$ contains the physically relevant system dynamics, higher-tier ADOs encode non-Markovian memory effects. The coupled ADO hierarchy structure introduces significant computational complexity, and density matrix representations are not well-suited for the formalism involving time evolution of wave functions under effective Hamiltonians. These can make it more complicated than wave function-based methods, the latter based on Schrödinger-type equations. Crucially, these limitations motivate a transformation of eqs 7 and 8 into Schrödinger-like equations to bypass both ADOs coupling and density matrix constraints.

The presence of operators acting right of ADOs in eqs 7 and 9 necessitates operator reordering to derive a Schrödinger-like equation. Following Borrelli's twin space formalism, 80 we implement this by extending the Liouville space: for a physical system with orthonormal basis $\{|m\rangle\}$ in Hilbert space H, we introduce a dual basis $\{|\tilde{m}|\}$ in twin space \tilde{H} . Then, the identity vector of the space $H \otimes \tilde{H}$ is defined as

$$|I\rangle = \sum_{m} |m\tilde{m}\rangle \tag{11}$$

This enables vectorization of any density matrix through the following mapping:

$$\rho |I\rangle = \sum_{nm} C_{nm} |n\rangle \langle m|I\rangle = \sum_{nm} C_{nm} |n\rangle |\tilde{m}\rangle$$
(12)

We employ an occupation number representation for multisite electron/spin problems. The identity vector (eq 11) and transformed operators become:

$$|I\rangle = \prod_{i} \sum_{m_{i}} |m_{i}\tilde{m}_{i}\rangle = \sum_{\{m_{i}\}} \prod_{i} |m_{i}\tilde{m}_{i}\rangle \tag{13}$$

$$a_{i}^{\pm}\rho|I\rangle = a_{i}^{\pm}|\rho\rangle$$

$$\rho a_{i}^{\pm}|I\rangle = \rho\tilde{a}_{i}^{\mp}|I\rangle = \tilde{a}_{i}^{\mp}\rho|I\rangle = \tilde{a}_{i}^{\mp}|\rho\rangle$$

$$\sigma_{z}\rho|I\rangle = \sigma_{z}|\rho\rangle$$

$$\rho\sigma_{z}|I\rangle = \rho\tilde{\sigma}_{z}|I\rangle = \tilde{\sigma}_{z}\rho|I\rangle = \tilde{\sigma}_{z}|\rho\rangle$$
(14)

$$|\rho\rangle = \sum_{\{m_i\tilde{n}_i\}} C_{m_1\tilde{n}_1\cdots m_N\tilde{n}_N} \prod_i |m_i\tilde{n}_i\rangle \tag{15}$$

Critically, eq 14 positions all operators left of ADOs within the space $H \otimes \tilde{H}$, distinct from the original Hilbert space. For single-electron systems, a_i^+ , a_i represent hard-core boson or spin operators satisfying commutation relation with ρ . This differs from Lindblad-based approaches (see Section S2 for full derivation). Cases requiring explicit antisymmetry properties for many-electron systems will be addressed in subsequent work. The vectorized state $|\rho\rangle$ in eq 15 exhibits a natural MPS structure, enabling direct compatibility with MPS calculations.

Applying the transformation in eq 14to eqs 7 and 9 yields

$$\begin{split} |\dot{\rho_{n}}\rangle &= -\bigg(iL_{S} + \sum_{k} n_{k}\gamma_{k}\bigg)|\rho_{n}\rangle - i\sum_{k} (\sigma_{z} - \tilde{\sigma}_{z})|\rho_{n_{ik}^{+}}\rangle \\ &- i\sum_{k} n_{k}(\eta_{k}\sigma_{z} - \eta_{k}^{*}\tilde{\sigma}_{z})|\rho_{n_{ik}^{-}}\rangle \\ |\dot{\rho_{n}}\rangle &= -\bigg(iL_{S} + \sum_{i}^{N} \sum_{k} n_{ik}\gamma_{ik}\bigg)|\rho_{n}\rangle - i\sum_{i}^{N} \sum_{k} (a_{i}^{+}a_{i} - \tilde{a}_{i}^{+}\tilde{a}_{i}) \\ |\rho_{n_{ik}^{+}}\rangle - i\sum_{i}^{N} \sum_{k} n_{ik}(\eta_{k}a_{i}^{+}a_{i} - \eta_{k}^{*}\tilde{a}_{i}^{+}\tilde{a}_{i})|\rho_{n_{ik}^{-}}\rangle \end{split}$$

$$(16)$$

Note that in eq 3, η_k has the dimension of energy squared (since the spectral density function has the dimension), while γ_k maintains energy/frequency dimension. Therefore, $\{\rho_n\}$ have different dimensions and we introduce a scaling parameter $\prod_k (|\eta_k|^{n_k} n_k!)^{-1/2}$, transforming eq 16 into:

$$\begin{split} |\dot{\rho_{n}}\rangle &= -\Bigg[iL_{S} + \sum_{k} n_{k}\gamma_{k}\Bigg]|\rho_{n}\rangle \\ -i\sum_{k} (\sigma_{z} - \tilde{\sigma}_{z})\sqrt{(n_{k} + 1)|\eta_{k}|}|\rho_{n_{ik}^{+}}\rangle \\ -i\sum_{k} \sqrt{n_{k}/|\eta_{k}|}(\eta_{k}\sigma_{z} - \eta_{k}^{*}\tilde{\sigma}_{z})|\rho_{n_{ik}^{-}}\rangle \\ |\dot{\rho_{n}}\rangle &= -\Bigg[iL_{S} + \sum_{i}^{N} \sum_{k} n_{ik}\gamma_{ik}\Bigg]|\rho_{n}\rangle \\ -i\sum_{i}^{N} \sum_{k} (a_{i}^{+}a_{i} - \tilde{a}_{i}^{+}\tilde{a}_{i})\sqrt{(n_{ik} + 1)|\eta_{k}|}|\rho_{n_{ik}^{+}}\rangle \\ -i\sum_{i}^{N} \sum_{k} \sqrt{n_{ik}/|\eta_{k}|}(\eta_{k}a_{i}^{+}a_{i} - \eta_{k}^{*}\tilde{a}_{i}^{+}\tilde{a}_{i})|\rho_{n_{ik}^{-}}\rangle \end{split}$$

$$(17)$$

In eq 17, the terms involving n_k , $\sqrt{n_k}$, $\sqrt{n_k+1}$ exhibit formal equivalence to bosonic creation and annihilation operators. To further simplify the structure, we introduce a virtual bosonic space:

$$|n\rangle = |n_1 n_2 \cdots n_I\rangle = (b_1^+)^{n_1} (b_2^+)^{n_2} \cdots (b_I^+)^{n_L} |00 \cdots 0\rangle \tag{18}$$

governed by virtual operators satisfying standard phonon bosonic algebra:

$$b_i^+|n\rangle = \sqrt{n_i + 1} |n + 1_i\rangle$$

$$b_i|n\rangle = \sqrt{n_i} |n - 1_i\rangle$$
(19)

This motivates replacing hierarchical *n*-dependent terms with phonon operators. We introduce a unified state

combining space $|\rho_n(t)\rangle$ (eq 16) and virtual bosonic space $|n\rangle$ (eq 18):

$$|\Psi(t)\rangle = \sum_{n} |\rho_{n}(t)\rangle \otimes |n\rangle$$

$$= \sum_{m_{1}\tilde{m}_{1}\cdots m_{N}\tilde{m}_{N}} C_{m_{1}\tilde{m}_{1}\cdots m_{N}\tilde{m}_{N}}^{n}(t)|m_{1}\tilde{m}_{1}\cdots m_{N}\tilde{m}_{N}\rangle \otimes |n\rangle$$
(20)

Applying the FMO HEOM equation (eq 9) as an example, the time evolution becomes

$$i\frac{\mathrm{d}}{\mathrm{d}t}|\Psi(t)\rangle = i\frac{\mathrm{d}}{\mathrm{d}t}\sum_{n}|\rho_{n}(t)\rangle\otimes|n\rangle$$

$$=i\sum_{n}\left\{-\left(iL_{S} + \sum_{i}^{N}\sum_{k}n_{ik}\gamma_{ik}\right)|\rho_{n}\rangle$$

$$-i\sum_{i}^{N}\sum_{k}\sqrt{(n_{ik}+1)|\eta_{k}|}\left(a_{i}^{+}a_{i} - \tilde{a}_{i}^{+}\tilde{a}_{i}\right)|\rho_{n_{ik}^{+}}\rangle$$

$$-i\sum_{i}^{N}\sum_{k}\sqrt{n_{ik}/|\eta_{k}|}\left(\eta_{k}a_{i}^{+}a_{i} - \eta_{k}^{*}\tilde{a}_{i}^{+}\tilde{a}_{i}\right)|\rho_{n_{ik}^{-}}\rangle\}\otimes|n\rangle$$

$$=\sum_{n}\left\{H_{S} - \tilde{H}_{S} - i\sum_{ik}\gamma_{ik}b_{ik}^{+}b_{ik}|\rho_{n}\rangle\otimes|n\rangle$$

$$+\sum_{ik}\sqrt{|\eta_{k}|}\left(a_{i}^{+}a_{i}b_{ik} - b_{ik}\tilde{a}_{i}^{+}\tilde{a}_{i}\right)|\rho_{n_{ik}^{+}}\rangle\otimes|n_{ik}^{+}\rangle$$

$$+\sum_{ik}\frac{1}{\sqrt{|\eta_{k}|}}\left(\eta_{k}a_{i}^{+}a_{i}b_{ik}^{+} - \eta_{k}^{*}b_{ik}^{+}\tilde{a}_{i}^{+}\tilde{a}_{i}\right)|\rho_{n_{ik}^{-}}\rangle\otimes|n_{ik}^{-}\rangle\}$$

$$=\left\{H_{S} - \tilde{H}_{S} - i\sum_{ik}\gamma_{ik}b_{ik}^{+}b_{ik} + \sum_{ik}\sqrt{|\eta_{k}|}\left(a_{i}^{+}a_{i}b_{ik} - b_{ik}\tilde{a}_{i}^{+}\tilde{a}_{i}\right) + \sum_{ik}\frac{1}{\sqrt{|\eta_{k}|}}\left(\eta_{k}a_{i}^{+}a_{i}b_{ik}^{+} - \eta_{k}^{*}b_{ik}^{+}\tilde{a}_{i}^{+}\tilde{a}_{i}\right)\right\}|\Psi(t)\rangle$$

$$(21)$$

Therefore, this reformulates HEOM into a Schrödinger-like equation with an effective Hamiltonian, and model-specific realizations are as follows:

$$i\frac{\mathrm{d}}{\mathrm{d}t}|\Psi(t)\rangle = H_{\mathrm{eff}}|\Psi(t)\rangle$$

$$H_{\mathrm{eff}} = H_{\mathrm{S}} - i\sum_{k} \gamma_{k} b_{k}^{+} b_{k} + \sum_{k} \sqrt{|\eta_{k}|} (\sigma_{z} b_{k} - b_{k} \tilde{\sigma}_{z})$$

$$+ \sum_{k} \frac{1}{\sqrt{|\eta_{k}|}} (\eta_{k} \sigma_{z} b_{k}^{+} - \eta_{k}^{*} b_{k}^{+} \tilde{\sigma}_{z})$$

$$(23)$$

for the spin-boson model;

$$H_{\text{eff}} = H_{S} - \tilde{H}_{S} - i \sum_{ik} \gamma_{ik} b_{ik}^{+} b_{ik}$$

$$+ \sum_{ik} \sqrt{|\eta_{k}|} (a_{i}^{+} a_{i} b_{ik} - b_{ik} \tilde{a}_{i}^{+} \tilde{a}_{i})$$

$$+ \sum_{ik} \frac{1}{\sqrt{|\eta_{k}|}} (\eta_{k} a_{i}^{+} a_{i} b_{ik}^{+} - \eta_{k}^{*} b_{ik}^{+} \tilde{a}_{i}^{+} \tilde{a}_{i})$$
(24)

for FMO, and;

$$H_{\text{eff}} = H_{\text{S}} - \tilde{H}_{\text{S}} - i \sum_{ik} \gamma_{ik} b_{ik}^{\dagger} b_{ik}$$

$$+ \sum_{ik} \sqrt{|\eta_{k}|} \left[(a_{i}^{+} a_{i+1} + a_{i+1}^{+} a_{i}) b_{ik} - b_{ik} (\tilde{a}_{i}^{+} \tilde{a}_{i+1} + \tilde{a}_{i+1}^{+} \tilde{a}_{i}) \right]$$

$$+ \sum_{ik} \frac{1}{\sqrt{|\eta_{k}|}} \left[\eta_{k} (a_{i}^{+} a_{i+1} + a_{i+1}^{+} a_{i}) b_{ik}^{+} - \eta_{k}^{*} b_{ik}^{+} (\tilde{a}_{i}^{+} \tilde{a}_{i+1} + \tilde{a}_{i+1}^{+} \tilde{a}_{i}) \right]$$
(25)

for the Peierls model.

pubs.acs.org/JCTC

With these effective Hamiltonians established, we compute population dynamics via

$$\langle \sigma_{z}(t) \rangle = \operatorname{Tr}(\rho \sigma_{z}(t)) = \langle I_{0} | \sigma_{z} | \Psi(t) \rangle$$
$$\langle N_{i}(t) \rangle = \operatorname{Tr}(\rho N_{i}(t)) = \langle I_{0} | a_{i}^{+} a_{i} | \Psi(t) \rangle$$
(26)

where $|I_0\rangle = \prod_i \sum_{m_i} |m_i \tilde{m}_i\rangle \otimes |n = \vec{0}\rangle$ sets the system in a maximally entangled state and virtual phonons in their ground state. Section 2.3 details the MPS implementation of this time evolution.

2.3. HEOM in MPS Format. 2.3.1. MPS and MPO. The MPS ansatz provides a natural framework for solving the timedependent Schrödinger-like equation (eq 22) governed by the effective Hamiltonians in eqs 23-25. Within the MPS formalism, 40,66,81 any quantum state is represented as a chain product of matrices:

$$|\Psi\rangle = \sum_{\{a\},\{\sigma\}} A[1]_{a_1}^{\sigma_1} A[2]_{a_1 a_2}^{\sigma_2} \cdots A[n]_{a_{n-1}}^{\sigma_n} |\sigma_1 \sigma_2 \cdots \sigma_n\rangle$$
(27)

where A[i] denotes matrices for the *i*th physical bond σ_{i} with the *i*th virtual bond a_i connecting adjacent matrices as shown in Figure 1a. The direct structural correspondence between eqs 20 and 27 demonstrates the inherent compatibility of MPS with our twin space formulation.

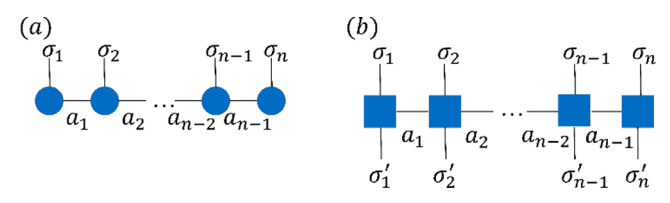


Figure 1. Schematic diagram of (a) MPS and (b) MPO. $\{\sigma, \sigma'\}$ are physical bonds and $\{a\}$ are virtual bonds.

Similarly, quantum operators are represented as Matrix Product Operators (MPOs) through a tensor network

$$\hat{O} = \sum_{\{a\},\{\sigma\},\{\sigma'\}} W[1]_{a_1}^{\sigma_1 \sigma'_1} W[2]_{a_1 a_2}^{\sigma_2 \sigma'_2} \cdots W[n]_{a_{n-1}}^{\sigma_n \sigma'_n} |\sigma_1 \sigma_2 \cdots \sigma_n\rangle$$

$$\langle \sigma'_1 \sigma'_2 \cdots \sigma'_n | \qquad (28)$$

where W[i] denotes operator matrices for the *i*-th physical bond σ_i , σ'_i , with the *i*th virtual bond a_i connecting adjacent sites, as shown in Figure 1b.

The power of tensor network methods lies in their ability to near-exactly describe many-body entanglement through controlled truncation of small singular values across virtual bonds, thereby reducing computational scaling from exponential to polynomial scaling.⁶⁶

2.3.2. Time Evolution Algorithm. To solve the time-dependent Schrödinger-like equation, we employ the time-dependent variational principle for time evolution. The Dirac-Frenkel time-dependent variational principle is expressed as

$$\langle \delta \Psi | i \frac{\partial}{\partial t} - \hat{H} | \Psi \rangle = 0 \tag{29}$$

This variational procedure projects the wave function's time derivative onto the MPS manifold, constrained by the fixed virtual bond dimension. Using the manifold's projection operator, the equation becomes

$$\frac{\partial |\Psi(t)\rangle}{\partial t} = -i\hat{P}\hat{H}|\Psi(t)\rangle \tag{30}$$

$$\hat{P} = \sum_{i=1}^{n} \hat{P}[1: i - 1] \otimes \hat{I}_{i} \otimes \hat{P}[i + 1: n]$$

$$- \sum_{i=1}^{n-1} \hat{P}[1: i] \otimes \hat{P}[i + 1: n]$$
(31)

where \hat{P} is the projection operator 72,84,85

$$\hat{P}[1:i] = \sum_{a,a'_i} |a'_i[1:i]\rangle S[1:i]_{a'_i a_i}^{-1} \langle a_i[1:i]|$$
(32)

$$\hat{P}[i+1:n] = \sum_{a,a'_i} |a'_i[i+1:n]\rangle S[i+1:n]_{a'_ia_i}^{-1} \langle a_i[i+1:n]|$$
(33)

$$\hat{I}_{i} = \sum_{\sigma_{i}} |\sigma_{i}\rangle\langle\sigma_{i}| \tag{34}$$

$$\hat{P}[1:0] = \hat{P}[n+1:n] = 1 \tag{35}$$

Here, S denotes the overlap matrix when the renormalized bases are nonorthogonal. Equation 31 equivalently represents a projection onto the tangent space of $|\Psi(t)\rangle$. For a small time Δt , the wave function in eq 30 has the formal solution:

$$|\Psi(t + \Delta t)\rangle = e^{-i\hat{p}\hat{H}\Delta t}|\Psi(t)\rangle$$
 (36)

This process is iterated for long-time evolution t with Δt carefully tested to ensure convergence.

At 0 K, the expectation value of any operator $\hat{F}(t)$ is

$$\langle \hat{F}(t) \rangle = \langle \Psi(0) | e^{i\hat{H}t} \hat{F} e^{-i\hat{H}t} | \Psi(0) \rangle$$
 (37)

where time evolution follows eq 36 numerically. In this work, however, we address finite-temperature problems using the reduced density matrix formalism. The general expectation value is therefore given by eq 26:

$$\langle \hat{F}(t) \rangle = \langle I_0 | \hat{F} | \Psi(t) \rangle = \langle I_0 | \hat{F} e^{-i\hat{H}_{\text{eff}}t} | \Psi(0) \rangle$$
 (38)

2.3.3. Particle Conservation. The Holstein—Peierls model describes a single electron in the system coupled to phonons. Its formulation uses the occupation number representation or the conventional Fock space and constrains the electron number to unity throughout the entire process. In contrast, the spin-boson model describes a two-level system coupled to a bosonic environment or a bosonic bath. Its basis states represent occupancy of either one level or the other and not the population of a specific site. Consequently, we can impose

and leverage U1 symmetry to preserve particle conservation in the Holstein/Peierls model.

To satisfy this single-electron constraint, the maximally entangled state can lie within the single-electron subspace $|I_0\rangle=\sum_i|0_1\tilde{0}_1\cdots 0_{i-1}\tilde{0}_{i-1}1_i\tilde{1}_i0_{i+1}\tilde{0}_{i+1}\cdots 0_N\tilde{0}_N\rangle\otimes|n=\vec{0}\rangle$. For the spin-boson model, $|I_0\rangle=\Pi_i(|0_i\tilde{0}_i\rangle+|1_i\tilde{1}_i\rangle)\otimes|n=\vec{0}\rangle$. The initial states for the models are provided in Section 3.

2.3.4. Ordering of Degrees of Freedom. Although environmental issues have been addressed, the ordering scheme remains a significant consideration.^{33,39,40,44} We adopted the two ordering schemes illustrated in Figure 2. For the spin-

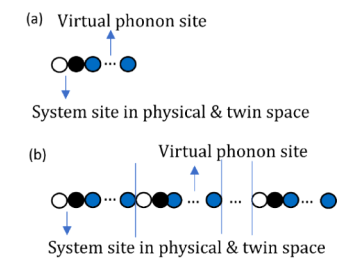


Figure 2. Schematic diagrams of the model configurations: (a) Spin-boson model; (b) Holstein/Peierls model. The blue circles represent virtual phonons, while white and black circles represent system sites in physical and twin space, respectively.

boson model (Figure 2a), the system part contains only two system sites, followed by virtual phonon sites. Here, each physical site is paired with its auxiliary counterpart to minimize long-range interactions. For the Holstein—Peierls model (Figure 2b), the ordering consists of N replications of the structure in Figure 2a. White circles represent physical system sites, each followed by their corresponding black auxiliary sites, and blue circles denote virtual phonon sites.

Similar ordering problems were encountered in our previous work, ^{33,42} using TFD formalism for finite-temperature electron—phonon coupling. However, TFD requires doubling of all physical phonon modes, which are discretized from the continuous spectral density. In contrast, for open quantum dynamics combined with MPS, only the system sites need duplication, followed by virtual phonon modes, which may not correspond directly to physical phonon modes. Furthermore, for the Holstein/Peierls model, the presence of only one electron allows us to merge all electronic sites into a single site, significantly enhancing computational efficiency⁴² in Section 3.3.

3. RESULTS AND DISCUSSION

We employ Padé decomposition of eq 3 to circumvent the Markovian approximation in Matsubara decomposition 62 throughout this work, unless otherwise specified. Decomposition parameters are provided in Section S3. Subsequently, we analyze the applicability of the three distinct models introduced in Section 2.1.

3.1. Spin-Boson Model. The spin-boson model describes a broad spectrum of phenomena, including charge-energy transfer, polaron dynamics, vibrational relaxation, and spin decoherence, among others. It represents a two-level system coupled to phonon modes, with the Hamiltonian defined in eq 4. Schematic representations are depicted in Figures 2a and 3. Population dynamics presented in Figure 4 employ parameters from ref 62, with $\varepsilon = 0$, $\Delta = 1$ in eq 4, $\lambda = 5$, ω_c



Figure 3. Spin-boson model: Diagrammatic representation. The system comprises two electronic levels yet is mathematically described through a single-site Hamiltonian.

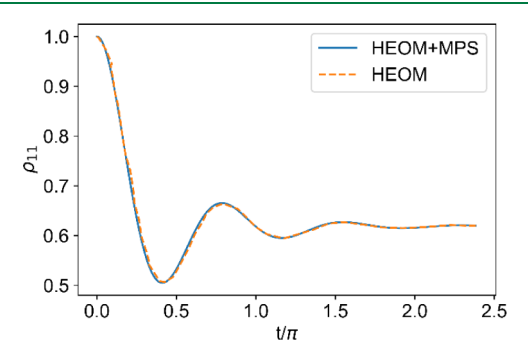


Figure 4. Time-dependent donor-state population validated against HEOM results.⁶²

= 0.25 in eq 6, and temperature β = 1. Results demonstrate quantitative agreement with HEOM, ⁶² confirming the accuracy of our HEOM-MPS hybrid approach. Time-dependent MPS parameters include: time step Δt = 0.005, bond dimension M = 50, and virtual phonon basis size equals 25. Spectral decomposition utilizes 7 Matsubara modes under the Markovian approximation (see Section S3).

3.2. FMO and Frenkel-Holstein Model.

$$J = \begin{bmatrix} 12410 & -87.7 & 5.5 & -5.9 & 6.7 & -13.7 & -9.9 \\ -87.7 & 12530 & 30.8 & 8.2 & 0.7 & 11.8 & 4.3 \\ 5.5 & 30.8 & 12210 & -53.5 & -2.2 & -9.6 & 6 \\ -5.9 & 8.2 & -53.5 & 12320 & -70.7 & -17 & -63.3 \\ 6.7 & 0.7 & -2.2 & -70.7 & 12480 & 81.1 & -1.3 \\ -13.7 & 11.8 & -9.6 & -17 & 81.1 & 12630 & 39.7 \\ -9.9 & 4.3 & 6 & -63.3 & -1.3 & 39.7 & 12440 \\ (39) & (3$$

To demonstrate the efficacy of our HEOM + MPS methodology, we examine excitation energy transfer in the seven-site FMO complex—a canonical model for photosynthetic energy transduction. The system Hamiltonian (eq 9) and schematic representation (Figures 2b and 5) are provided, with site energies and electronic couplings, ⁷⁸ as shown in eq 39 in the unit of cm⁻¹. Additional parameters ⁷⁸ are $\lambda = 70$ cm⁻¹, $\omega_c^{-1} = 35$ fs, T = 300 K.

Population dynamics for all seven sites using the conventional Fock space method are presented in Figure 6a (see Section 3.3 for details), and the results demonstrate quantitative agreement with HEOM.⁷⁸ Time-dependent MPS parameters: time step $\Delta t = 3$ a.u, bond dimension M = 100, virtual phonon basis size equals 10. Spectral density decomposition employs 5 Padé modes (see Section S3).

3.3. The Ordering and Basis for HEOM + MPS in State-Vector Space. We analyze potential improvements to Figure 2b's tensor network structure: performance, efficiency, and accuracy of MPS are optimized under low-entanglement conditions 41,42,87–89 and deteriorated with long-range entan-

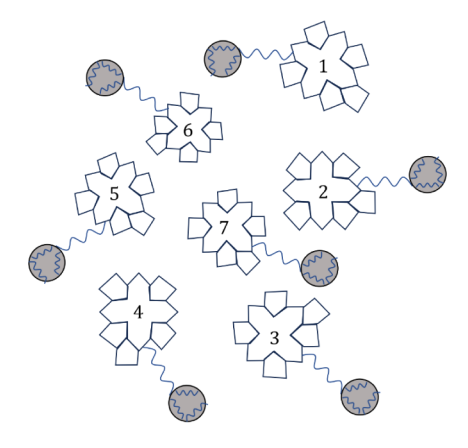


Figure 5. Schematic plot of the seven-site FMO complex. Primary excitation transfer pathways: $1 \rightarrow 2 \rightarrow 3$ and $6 \rightarrow 5/7 \rightarrow 4 \rightarrow 3$. Wavy lines denote intramolecular phonon modes at each site.

glement. In the current configuration, electronic degrees of freedom are separated by phonon modes—a suboptimal arrangement exacerbated by more phonon modes.⁴² Crucially, the FMO model represents a single-excitation subspace with precisely 7 electronic states (degrees of freedom equal 7 for this situation). While site-based ordering in conventional Fock space, followed by U1 symmetry restriction remains possible, the explicit mixing of electronic sites into a state-vector space constitutes a more efficient approach by

- (i) minimizing electron—phonon entanglements
- (ii) leveraging the single-excitation Hilbert space reduction.

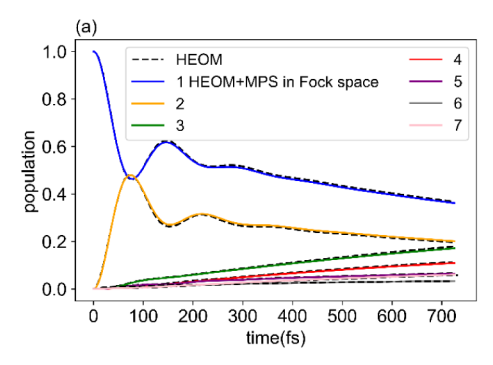
The spin-boson model, formulated in a one site within two-level space rather than with 2 sites' electronic creation/annihilation operators, actually operates within a state-vector space. Here, the single system site directly represents the occupation of either one of the two states.

This approach was previously implemented using discretized phonon modes in TFD + MPS.⁴² However, in the HEOM + MPS framework—where twin space duplicates the system's electronic degrees of freedom and duplicates the number of electrons in the original system—we must explicitly account for the anticommutation relations between physical space operators and their auxiliary counterparts. Therefore, the 14 electronic states (7 physical + 7 twin) cannot be indiscriminately combined.

We can establish the commutation relations between creation/annihilation operators in physical space and twin space, as derived in Section S2. This allows us to consolidate the seven physical space sites into a single composite site with a 7-dimensional basis and merge the seven twin space sites into another composite site with a 7-dimensional basis. This configuration—termed the state-vector space—contrasts with the conventional Fock space approach, where each site represents an individual electronic orbital. Schematic representations are provided in Figure 7.

Figure 6 compares the state-vector space and Fock space results for the FMO model under identical parameters. Both schemes exhibit negligible convergence differences at bond dimension M=100. We quantify numerical error as

$$\operatorname{Error}(t) = \sum_{i=1}^{7} |P_i(t) - P_{i, \operatorname{standard}}(t)|$$
(40)



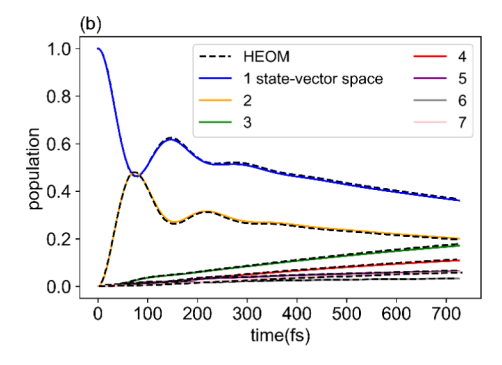


Figure 6. Time-dependent occupation numbers of the seven sites in the FMO model. We take (a) conventional Fock space restricted in U1 symmetry and (b) state-vector space configurations for HEOM + MPS calculations, as shown in Section 3.3. The results are compared with HEOM calculations.

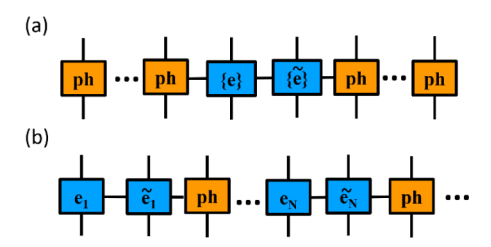


Figure 7. Schematic representations of basis schemes for HEOM + MPS. (a) State-vector space: blue sites denote electronic degrees in physical and twin spaces. Orange sites represent virtual phonon sites. (b) Conventional Fock space: 2N electronic states (N = 7 for FMO) with proximal arrangement of system sites and auxiliary counterparts to minimize long-range entanglement.

where the reference standard uses HEOM + MPS in statevector space with $\Delta t = 5$ a.u, bond dimension M = 150, Padé modes count 5, and virtual phonon basis size of 12. The corresponding error analysis is presented in Figure 8.

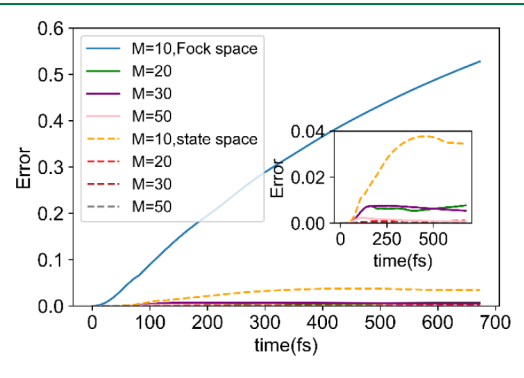


Figure 8. Time-dependent error for FMO model simulations comparing state-vector and Fock space schemes across bond dimensions. Fixed parameters: $\Delta t = 10$ a.u, Padé modes count 4, and virtual phonon basis of 10. Reference standard: state-vector space HEOM + MPS with $\Delta t = 5$ a.u, bond dimension M = 150, Padé modes count 5, and virtual phonon basis of 12.

In Figure 8, the conventional Fock space method simulations at bond dimension M = 10 exhibit more than 50% relative error. Conversely, the state-vector space method achieves less than 4% error under identical conditions. Even at M = 20-30, the Fock space configuration maintains more than 0.7% error, only falling below 0.2% at M = 50. The state-vector space scheme attains comparable accuracy at M = 20, with M =30 outperforming the Fock space method at M = 50. These

results demonstrate the significant advantages of the statevector space scheme over the conventional Fock space approach in terms of computational efficiency and accuracy.

3.4. HEOM + MPS Vs TFD + MPS. This section contrasts HEOM + MPS (rooted in open quantum dynamics) with TFD + MPS (employing a holistic system-environment treatment), both addressing finite-temperature problems under initially disentangled system-bath conditions.

We first define the time-evolving effective Hamiltonians:

$$\begin{split} H_{\text{eff}}^{\text{HEOM}} &= H_{\text{S}} - \tilde{H}_{\text{S}} - i \sum_{ik} \gamma_{ik} b_{ik}^{+} b_{ik} \\ &+ \sum_{ik} \sqrt{|\eta_{k}|} \, b_{ik} (a_{i}^{+} a_{i} - \tilde{a}_{i}^{+} \tilde{a}_{i}) \\ &+ \sum_{ik} \frac{1}{\sqrt{|\eta_{k}|}} b_{ik}^{+} (\eta_{k} a_{i}^{+} a_{i} - \eta_{k}^{*} \tilde{a}_{i}^{+} \tilde{a}_{i}) \end{split} \tag{41}$$

$$H_{\rm eff}^{\rm TFD} = e^{iG_{\rm B}} H e^{-iG_{\rm B}}$$

$$=H_{S} + \sum_{ik} \omega_{k} (b_{ik}^{+} b_{ik} - \tilde{b}_{ik}^{+} \tilde{b}_{ik}) + \sum_{ik} \cosh \theta_{k} g_{k} \omega_{k} a_{i}^{+}$$

$$a_{i} (b_{ik}^{+} + b_{ik}) + \sum_{ik} \sinh \theta_{k} g_{k} \omega_{k} a_{i}^{+} a_{i} (\tilde{b}_{ik}^{+} + \tilde{b}_{ik})$$
(42)

where
$$\theta_k = \arctan h(e^{-\beta\omega_k/2})$$
, and

 $G_{\rm B} = -i\sum_{ik}\theta_k(b_{ik}\tilde{b}_{ik} - b_{ik}^+\tilde{b}_{ik}^+)$ denotes the bosonic unitary transformation operator. Derivations of eq 42 follow established methodology. 33,42,75 Crucially, TFD + MPS requires auxiliary sites only for environmental phononswithout twin spaces of the system—contrasting with HEOM + MPS's dual-space architecture. Figure 9 illustrates the MPS configurations for TFD + MPS, enabling a direct intuitive comparison with HEOM + MPS.

Second, to discretize the Debye spectral density, we implement the following discretization schemes:^{33,90}

$$\rho(\omega) = \frac{2(N+1)}{\pi} \frac{\omega_{\rm c}}{\omega_{\rm c}^2 + \omega^2} \tag{43}$$

$$\int_0^{\omega_j} d\omega \rho(\omega) = j, \quad j = 1, 2, \dots, N$$
(44)

$$\omega_{j} = \omega_{c} \tan \frac{j\pi}{2(N+1)} \tag{45}$$

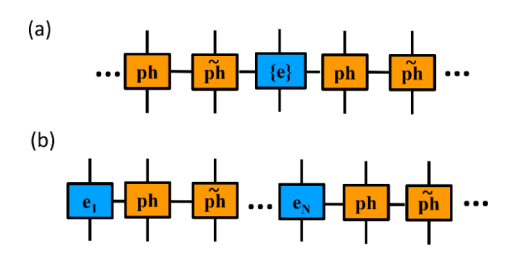


Figure 9. Basis scheme representations for the TFD + MPS. (a) Statevector space: blue site denotes the consolidated electronic system. Orange sites represent discretized phonon modes and their thermofield auxiliary counterparts. (b) Fock space: N electronic states with proximal arrangement of discretized phonon modes and auxiliary modes (orange sites). (N = 7).

$$g_{j} = \frac{c_{j}}{\sqrt{2\omega_{j}^{3}}} = \frac{1}{\sqrt{2\omega_{j}^{3}}} \sqrt{\frac{2}{\pi}\omega_{j} \frac{J(\omega_{j})}{\rho(\omega_{j})}} = \sqrt{\frac{\lambda}{2(N+1)\omega_{j}}}$$
(46)

Figure 10 compares HEOM + MPS and TFD + MPS performance for the state-vector space method. HEOM + MPS

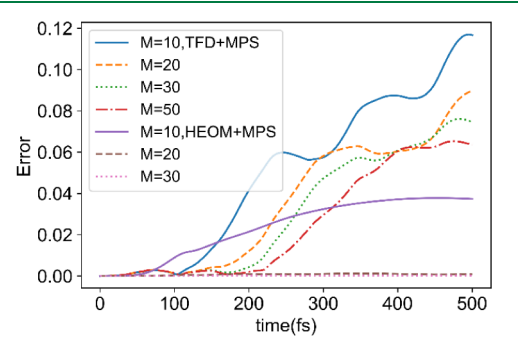


Figure 10. Time-dependent error comparison for HEOM + MPS vs TFD + MPS (state-vector space) across bond dimensions. HEOM + MPS parameters and reference standard are identical to those in Figure 8. TFD + MPS parameters are 70 discretized phonon modes: 35 physical +35 auxiliary modes.

parameters and reference standards match those in Figure 8. Fixed TFD + MPS parameters are $\Delta t = 10$ a.u and phonon basis equal to 10 (consistent with HEOM + MPS). Discretized modes count 35 physical modes and 70 effective modes (finitetemperature doubling). TFD + MPS exhibits a significantly slower convergence than HEOM + MPS for the Debye spectral density.

We compare HEOM + MPS with TFD + MPS using a complexity analysis. The number of parameters in the MPS wave function is polynomial with respect to the number of degrees of freedom, the number of MPS sites, and the square of the bond dimension. For the FMO model, the number of electronic sites and their associated degrees of freedom are fixed. In the HEOM + MPS approach, there are 14 electronic sites with a dimensionality of 2 each (conventional Fock space) but with only 2 sites of dimensionality 7 each in the state-vector space. In the TFD + MPS approach, there are 7 electronic sites of dimensionality 2 (conventional Fock space) and only 1 state-vector site of dimensionality 7 in the statevector space. These differences in the electronic part are relatively minor, particularly in the state-vector space representation. The main computational difference arises from the treatment of the phonons. With the phonon degrees of freedom per mode fixed at 10 as used in the main text, the HEOM + MPS method employs 4 virtual phonon sites per electronic site, resulting in a total of 28 virtual phonon sites. In contrast, the TFD + MPS method uses 35 physical and 35 auxiliary phonon sites per electronic site, leading to a total of 490 phonon sites. Furthermore, a larger number of sites and increased entanglement generally require a larger bond dimension, which further influences the computational cost.

It should be noted that although we compare HEOM + MPS and TFD + MPS in terms of computational complexity, their physical interpretations are fundamentally different. In HEOM + MPS, the virtual phonon sites originate from a mathematical construction based on the discretization of the bath correlation function; they obey bosonic commutation relations, and the method belongs to the family of open quantum dynamics methods. In TFD + MPS, the phonon sites represent real physical phonons, arising from discretization of the full quantum space and spectral density function.

Third, we examine the sensitivity of results to the number of discretized phonon modes. For HEOM + MPS, convergence is achieved with just 4 modes, yielding quantitatively accurate dynamics. In contrast, TFD + MPS requires more than 40 modes, even at short times (finite-temperature doubling) to approach convergence, as shown in Figure 11a. We can observe that at short times, the error is dominated by the number of phonon modes, where a higher number generally leads to better accuracy, as the influence of bond dimension

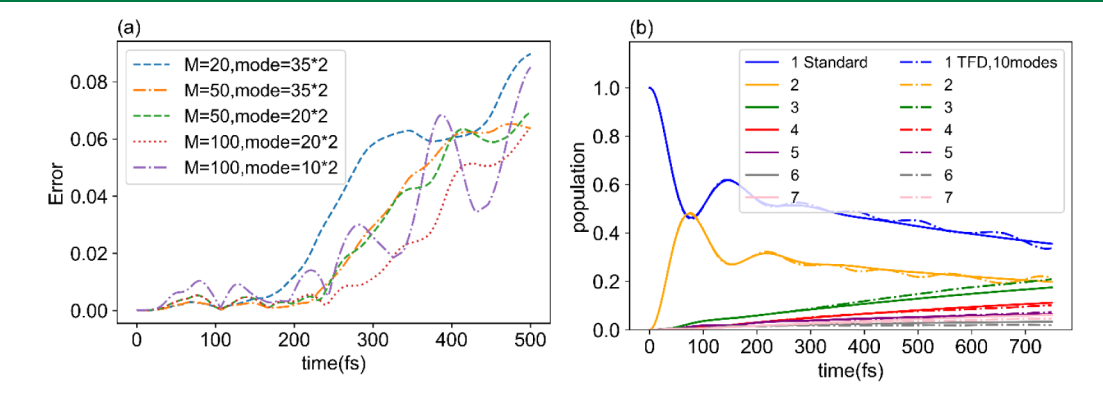


Figure 11. (a) Time-dependent error for TFD + MPS (state-vector space) in the FMO model: Bond dimension and phonon modes dependence. Parameters match those in Figure 10. (b) Site population dynamics: Reference standard and TFD + MPS with M = 100 and 20 discretized modes (10 physical +10 auxiliary).

and entanglement entropy remains limited. In contrast, at a longer evolution time, a small bond dimension results in the accumulation of truncation errors, leading to a significant increase in the overall error. Besides, insufficient modes induce unphysical artifacts, including spurious recurrences and persistent oscillations at extended time scales 33,36,91 both in Figure 11a and b.

Finally, we benchmarked computational efficiency for both methodologies. Using fixed parameters ($\Delta t = 10$ a.u., phonon basis equal to 10), we analyzed time evolution over 500 fs (2,067 time steps), as shown in Figure 12. HEOM + MPS

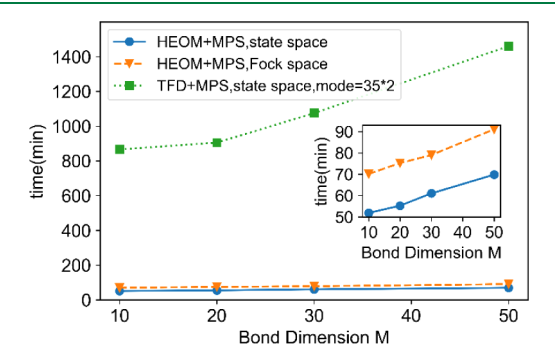


Figure 12. Computational time across methodologies for 500 fs evolution with $\Delta t = 10$ a.u. All calculations were performed on a virtual machine equipped with an Intel Xeon Platinum 8255C CPU @ 2.50 GHz, 4 cores, and 8 GB of RAM.

exhibits 22-27% faster execution in state-vector space than in conventional Fock space. In addition, both HEOM implementations outperform TFD by more than an order of magnitude in efficiency.

3.5. Peierls Model. We finally examine the Peierls model—distinguished from the Holstein model by its intermolecular electron-phonon coupling (Figure 13). Applying HEOM to this one-dimensional system, we simulate singleelectron diffusion with a Hamiltonian (eq 10) featuring nonlocal electron-phonon interactions and only nearestneighbor hopping. Initializing an electron at site 15 of a 31site chain, we track carrier diffusion via time-dependent and

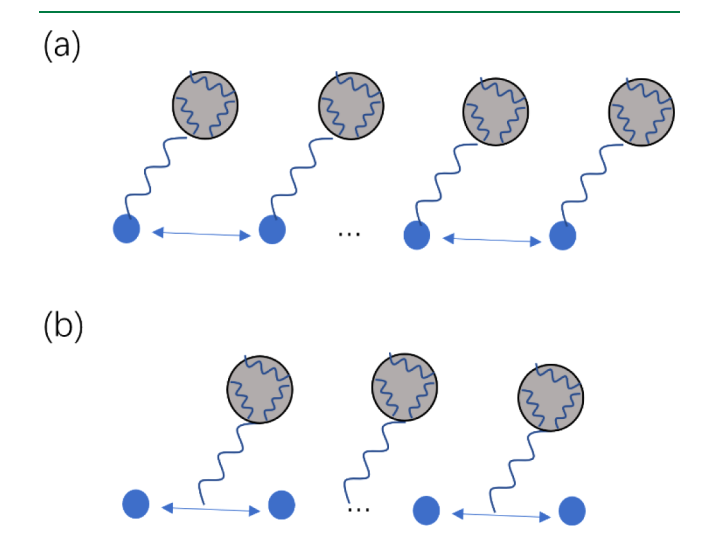


Figure 13. Schematic representations of (a) Holstein and (b) Peierls models. Peierls coupling manifested as intermolecular electronphonon coupling is explicitly encoded in eq 10.

site-resolved populations, computing mean square displacement (MSD):

$$MSD(t) = \langle \Delta r^{2}(t) \rangle - \langle \Delta r(t) \rangle^{2}$$

$$= \sum_{j} n_{j}(t)(j - j_{0})^{2} - \left[\sum_{j} n_{j}(t)(j - j_{0}) \right]^{2}$$
(47)

Parameters: $J = -300 \text{ cm}^{-1}$, $\varepsilon = 0$, $\lambda = 323 \text{ cm}^{-1}$, $\omega_c = 41$ cm⁻¹. Other parameters for HEOM+MPS are $\Delta t = 3$ a.u, bond dimension M = 100, Padé modes count 7, and virtual phonon basis size equal to 11. Figure 14 demonstrates robust agreement between our method and benchmark HEOM^{70,92} results, particularly at cryogenic temperatures.

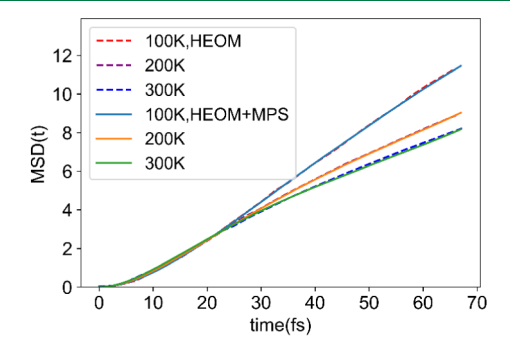


Figure 14. MSD of electron transport in a 31-site chain at different temperatures. Comparisons are between HEOM + MPS results and standard HEOM calculations.7

4. CONCLUSIONS

In this study, we employed the HEOM equation combined with MPS algorithms to investigate the time-dependent populations for organic molecular aggregates with electronphonon couplings. Calculations were performed for the spinboson model, the FMO model, and the Peierls diffusion model.

We first introduce the HEOM formulations. Since these equations are based on density matrices, we employ a twinspace representation to transform them into a Schrödinger-like equation. Using virtual phonon sites, we can decouple ADOs, yielding an effective Hamiltonian that combines naturally with MPS. The proposed HEOM + MPS methodology was rigorously validated across multiple models and parameter regimes. To validate the accuracy and efficiency of our method, we compared results with conventional HEOM and TFD + MPS. When compared with TFD + MPS, despite both methods utilizing auxiliary spaces and density matrices and are at finite temperature, HEOM + MPS demonstrates marked superiority in accuracy and computational efficiency. This advantage stems from fundamental differences in their effective Hamiltonians. Furthermore, we address configuration and ordering optimization problems, leveraging the U1 symmetry for single-electron systems to develop a state-vector space approach for HEOM + MPS. This implementation outperforms conventional Fock space representations. Finally, for the Peierls model, our method maintains high accuracy even at low temperatures, demonstrating robust applicability to general charge transport problems in dissipative bosonic environments.

This work primarily focuses on charge transport in molecular aggregates, bulk systems, and single-electron problems. A number of interesting issues, such as molecular junctions with dissipative fermionic environments, many-electron systems, spin/heat transport, and disorder problems, ^{42,93} remain to be further explored.

ASSOCIATED CONTENT

Supporting Information

The Supporting Information is available free of charge at https://pubs.acs.org/doi/10.1021/acs.jctc.5c01385.

Derivation of bath correlation functions; derivation of operators in twin space; Padé and Matsubara decomposition parameters (PDF)

AUTHOR INFORMATION

Corresponding Author

Zhigang Shuai — MOE Key Laboratory of Organic Optoelectronics and Molecular Engineering, Department of Chemistry, Tsinghua University, Beijing 100084, People's Republic of China; School of Science and Engineering, The Chinese University of Hong Kong, Shenzhen, Guangdong 518172, People's Republic of China; Guangdong Basic Research Center of Excellence for Aggregate Science, School of Science and Engineering, The Chinese University of Hong Kong, Shenzhen, Guangdong 518172, People's Republic of China; orcid.org/0000-0003-3867-2331; Email: shuaizhigang@cuhk.edu.cn

Authors

Hengrui Yang – MOE Key Laboratory of Organic Optoelectronics and Molecular Engineering, Department of Chemistry, Tsinghua University, Beijing 100084, People's Republic of China; orcid.org/0000-0001-8525-9772

Zirui Sheng — School of Science and Engineering, The Chinese University of Hong Kong, Shenzhen, Guangdong 518172, People's Republic of China; Guangdong Basic Research Center of Excellence for Aggregate Science, School of Science and Engineering, The Chinese University of Hong Kong, Shenzhen, Guangdong 518172, People's Republic of China

Liqi Zhou – MOE Key Laboratory of Organic Optoelectronics and Molecular Engineering, Department of Chemistry, Tsinghua University, Beijing 100084, People's Republic of China; orcid.org/0009-0002-3943-0959

Complete contact information is available at: https://pubs.acs.org/10.1021/acs.jctc.5c01385

Notes

The authors declare no competing financial interest.

ACKNOWLEDGMENTS

We are grateful to Profs. Qiang Shi, Jiajun Ren, Weitang Li, and Dr. Tianchu Li for numerous insightful discussions and help. This work is supported by the National Natural Science Foundation of China (Grant Nos. T2350009 and 22433007), the Guangdong Provincial Natural Science Foundation (Grant No. 2024A1515011185), and the Shenzhen City Peacock Team Project (Grant No. KQTD20240729102028011). Z. Shuai and Z. Sheng are supported by the Guangdong Basic Research Center of Excellence for Aggregate Science.

REFERENCES

(1) Schweicher, G.; Garbay, G.; Jouclas, R.; Vibert, F.; Devaux, F.; Geerts, Y. H. Molecular Semiconductors for Logic Operations: Dead-End or Bright Future? *Adv. Mater.* **2020**, *32* (10), 1905909.

- (2) Calió, L.; Kazim, S.; Grätzel, M.; Ahmad, S. Hole-Transport Materials for Perovskite Solar Cells. *Angew. Chem., Int. Ed.* **2016**, *55* (47), 14522–14545.
- (3) Bach, U.; Lupo, D.; Comte, P.; Moser, J. E.; Weissörtel, F.; Salbeck, J.; Spreitzer, H.; Grätzel, M. Solid-State Dye-Sensitized Mesoporous TiO2 Solar Cells with High Photon-to-Electron Conversion Efficiencies. *Nature* **1998**, 395 (6702), 583–585.
- (4) Tang, C. W.; Van Slyke, S. A. Organic Electroluminescent Diodes. *Appl. Phys. Lett.* **1987**, *51* (12), 913–915.
- (5) Chen, S.; Deng, L.; Xie, J.; Peng, L.; Xie, L.; Fan, Q.; Huang, W. Recent Developments in Top-Emitting Organic Light-Emitting Diodes. *Adv. Mater.* **2010**, 22 (46), 5227–5239.
- (6) Joachim, C.; Gimzewski, J. K.; Aviram, A. Electronics Using Hybrid-Molecular and Mono-Molecular Devices. *Nature* **2000**, *408* (6812), 541–548.
- (7) Chen, F.; Hihath, J.; Huang, Z.; Li, X.; Tao, N. J. Measurement of Single-Molecule Conductance. *Annu. Rev. Phys. Chem.* **2007**, *58* (1), *535–564*.
- (8) Galperin, M.; Ratner, M. A.; Nitzan, A.; Troisi, A. Nuclear Coupling and Polarization in Molecular Transport Junctions: Beyond Tunneling to Function. *Science* **2008**, *319* (5866), 1056–1060.
- (9) Nitzan, A. ELECTRON TRANSMISSION THROUGH MOLECULES AND MOLECULAR INTERFACES. *Annu. Rev. Phys. Chem.* **2001**, 52 (1), 681–750.
- (10) Selzer, Y.; Allara, D. L. SINGLE-MOLECULE ELECTRICAL JUNCTIONS. Annu. Rev. Phys. Chem. **2006**, *57* (1), 593–623.
- (11) Blülle, B.; Troisi, A.; Häusermann, R.; Batlogg, B. Charge Transport Perpendicular to the High Mobility Plane in Organic Crystals: Bandlike Temperature Dependence Maintained despite Hundredfold Anisotropy. *Phys. Rev. B* **2016**, 93 (3), 035205.
- (12) Glarum, S. H. Electron Mobilities in Organic Semiconductors. *J. Phys. Chem. Solids* **1963**, 24 (12), 1577–1583.
- (13) Xi, J.; Long, M.; Tang, L.; Wang, D.; Shuai, Z. First-Principles Prediction of Charge Mobility in Carbon and Organic Nanomaterials. *Nanoscale* **2012**, *4* (15), 4348.
- (14) Troisi, A. Charge Transport in High Mobility Molecular Semiconductors: Classical Models and New Theories. *Chem. Soc. Rev.* **2011**, 40 (5), 2347–2358.
- (15) Munn, R. W.; Silbey, R. Theory of Electronic Transport in Molecular Crystals. III. Diffusion Coefficient Incorporating Nonlocal Linear Electron–Phonon Coupling. *J. Chem. Phys* **1985**, *83* (4), 1854–1864.
- (16) Hannewald, K.; Bobbert, P. A. Anisotropy Effects in Phonon-Assisted Charge-Carrier Transport in Organic Molecular Crystals. *Phys. Rev. B* **2004**, *69* (7), 075212.
- (17) Fratini, S.; Mayou, D.; Ciuchi, S. The Transient Localization Scenario for Charge Transport in Crystalline Organic Materials. *Adv. Funct. Mater.* **2016**, *26* (14), 2292–2315.
- (18) Ciuchi, S.; Fratini, S.; Mayou, D. Transient Localization in Crystalline Organic Semiconductors. *Phys. Rev. B* **2011**, *83* (8), 081202.
- (19) Park, H.; Park, J.; Lim, A. K. L.; Anderson, E. H.; Alivisatos, A. P.; McEuen, P. L. Nanomechanical Oscillations in a Single-C60 Transistor. *Nature* **2000**, 407 (6800), 57–60.
- (20) Wang, L.; Nan, G.; Yang, X.; Peng, Q.; Li, Q.; Shuai, Z. Computational Methods for Design of Organic Materials with High Charge Mobility. *Chem. Soc. Rev.* **2010**, *39* (2), 423–434.
- (21) Troisi, A.; Orlandi, G. Charge-Transport Regime of Crystalline Organic Semiconductors: Diffusion Limited by Thermal Off-Diagonal Electronic Disorder. *Phys. Rev. Lett.* **2006**, *96* (8), 086601.
- (22) Wang, L.; Beljonne, D. Flexible Surface Hopping Approach to Model the Crossover from Hopping to Band-like Transport in Organic Crystals. *J. Phys. Chem. Lett.* **2013**, *4* (11), 1888–1894.
- (23) Giannini, S.; Carof, A.; Ellis, M.; Yang, H.; Ziogos, O. G.; Ghosh, S.; Blumberger, J. Quantum Localization and Delocalization of Charge Carriers in Organic Semiconducting Crystals. *Nat. Commun.* **2019**, *10* (1), 3843.

- (24) Nan, G.; Yang, X.; Wang, L.; Shuai, Z.; Zhao, Y. Nuclear Tunneling Effects of Charge Transport in Rubrene, Tetracene, and Pentacene. *Phys. Rev. B* **2009**, *79* (11), 115203.
- (25) Jiang, Y.; Zhong, X.; Shi, W.; Peng, Q.; Geng, H.; Zhao, Y.; Shuai, Z. Nuclear Quantum Tunnelling and Carrier Delocalization Effects to Bridge the Gap between Hopping and Bandlike Behaviors in Organic Semiconductors. *Nanoscale Horiz.* **2016**, *1* (1), 53–59.
- (26) Geng, H.; Peng, Q.; Wang, L.; Li, H.; Liao, Y.; Ma, Z.; Shuai, Z. Toward Quantitative Prediction of Charge Mobility in Organic Semiconductors: Tunneling Enabled Hopping Model. *Adv. Mater.* **2012**, 24 (26), 3568–3572.
- (27) Asadi, K.; Kronemeijer, A. J.; Cramer, T.; Jan Anton Koster, L.; Blom, P. W. M.; de Leeuw, D. M. Polaron Hopping Mediated by Nuclear Tunnelling in Semiconducting Polymers at High Carrier Density. *Nat. Commun.* **2013**, *4* (1), 1710.
- (28) Sakanoue, T.; Sirringhaus, H. Band-like Temperature Dependence of Mobility in a Solution-Processed Organic Semiconductor. *Nat. Mater.* **2010**, *9* (9), 736–740.
- (29) Ren, X.; Bruzek, M. J.; Hanifi, D. A.; Schulzetenberg, A.; Wu, Y.; Kim, C.-H.; Zhang, Z.; Johns, J. E.; Salleo, A.; Fratini, S.; Troisi, A.; Douglas, C. J.; Frisbie, C. D. Negative Isotope Effect on Field-Effect Hole Transport in Fully Substituted 13C-Rubrene. *Adv. Electron. Mater.* **2017**, 3 (4), 1700018.
- (30) Nguyen, Q. V.; Frisbie, C. D. Hopping Conductance in Molecular Wires Exhibits a Large Heavy-Atom Kinetic Isotope Effect. *J. Am. Chem. Soc.* **2021**, *143* (7), 2638–2643.
- (31) Li, W.; Ren, J.; Shuai, Z. A General Charge Transport Picture for Organic Semiconductors with Nonlocal Electron-Phonon Couplings. *Nat. Commun.* **2021**, *12* (1), 4260.
- (32) Ge, Y.; Li, W.; Ren, J.; Shuai, Z. Computational Method for Evaluating the Thermoelectric Power Factor for Organic Materials Modeled by the Holstein Model: A Time-Dependent Density Matrix Renormalization Group Formalism. *J. Chem. Theory Comput.* **2022**, *18* (11), 6437–6446.
- (33) Yang, H.; Li, W.; Ren, J.; Shuai, Z. Time-Dependent Density Matrix Renormalization Group Method for Quantum Transport with Phonon Coupling in Molecular Junction. *J. Chem. Theory Comput.* **2023**, *19* (19), 6070–6081.
- (34) Ge, Y.; Li, W.; Ren, J.; Shuai, Z. Roles of Nonlocal Electron-Phonon Coupling on the Electrical Conductivity and Seebeck Coefficient: A Time-Dependent DMRG Study. *Phys. Rev. B* **2024**, *110* (3), 035201.
- (35) Li, W.; Ren, J.; Yang, H.; Wang, H.; Shuai, Z. Optimal Tree Tensor Network Operators for Tensor Network Simulations: Applications to Open Quantum Systems. *J. Chem. Phys.* **2024**, *161* (5), 054116.
- (36) Li, W.; Ren, J.; Shuai, Z. Finite-Temperature TD-DMRG for the Carrier Mobility of Organic Semiconductors. *J. Phys. Chem. Lett.* **2020**, *11* (13), 4930–4936.
- (37) Wang, H.; Pshenichnyuk, I.; Härtle, R.; Thoss, M. Numerically Exact, Time-Dependent Treatment of Vibrationally Coupled Electron Transport in Single-Molecule Junctions. *J. Chem. Phys.* **2011**, *135* (24), 244506.
- (38) Wang, H.; Thoss, M. Numerically Exact, Time-Dependent Study of Correlated Electron Transport in Model Molecular Junctions. J. Chem. Phys. 2013, 138 (13), 134704.
- (39) Elenewski, J. É.; Wójtowicz, G.; Rams, M. M.; Zwolak, M. Performance of Reservoir Discretizations in Quantum Transport Simulations. J. Chem. Phys. 2021, 155 (12), 124117.
- (40) Ren, J.; Shuai, Z.; Kin-Lic Chan, G. Time-Dependent Density Matrix Renormalization Group Algorithms for Nearly Exact Absorption and Fluorescence Spectra of Molecular Aggregates at Both Zero and Finite Temperature. *J. Chem. Theory Comput.* **2018**, *14* (10), 5027–5039.
- (41) Li, W.; Ren, J.; Yang, H.; Shuai, Z. On the Fly Swapping Algorithm for Ordering of Degrees of Freedom in Density Matrix Renormalization Group. *J. Phys.: condens. Matter* **2022**, 34 (25), 254003.

- (42) Sheng, Z.; Jiang, T.; Li, W.; Shuai, Z. TD-DMRG Study of Exciton Dynamics with Both Thermal and Static Disorders for Fenna-Matthews-Olson Complex. *J. Chem. Theory Comput.* **2024**, 20 (15), 6470–6484.
- (43) Kohn, L.; Santoro, G. E. Efficient Mapping for Anderson Impurity Problems with Matrix Product States. *Phys. Rev. B* **2021**, *104* (1), 014303.
- (44) Rams, M. M.; Zwolak, M. Breaking the Entanglement Barrier: Tensor Network Simulation of Quantum Transport. *Phys. Rev. Lett.* **2020**, *124* (13), 137701.
- (45) He, Z.; Millis, A. J. Entanglement Entropy and Computational Complexity of the Anderson Impurity Model out of Equilibrium: Quench Dynamics. *Phys. Rev. B* **2017**, *96* (8), 085107.
- (46) Chen, X.; Duan, W. Quantum thermal transport and spin thermoelectrics in low-dimensional nano systems: application of nonequilibrium Green's function method. *Acta Phys. Sin.* **2015**, *64*, 186302.
- (47) Mitra, A.; Aleiner, I.; Millis, A. J. Phonon Effects in Molecular Transistors: Quantal and Classical Treatment. *Phys. Rev. B* **2004**, *69* (24), 245302.
- (48) Sowa, J. K.; Mol, J. A.; Briggs, G. A. D.; Gauger, E. M. Beyond Marcus Theory and the Landauer-Büttiker Approach in Molecular Junctions: A Unified Framework. *J. Chem. Phys.* **2018**, *149* (15), 154112.
- (49) Lindblad, G. On the Generators of Quantum Dynamical Semigroups. *Commun. Math. Phys.* **1976**, 48 (2), 119–130.
- (50) Dzhioev, A. A.; Kosov, D. S. Super-Fermion Representation of Quantum Kinetic Equations for the Electron Transport Problem. *J. Chem. Phys.* **2011**, *134* (4), 044121.
- (51) Wójtowicz, G.; Elenewski, J. E.; Rams, M. M.; Zwolak, M. Open-System Tensor Networks and Kramers' Crossover for Quantum Transport. *Phys. Rev. A* **2020**, *101* (5), 050301.
- (52) Manzano, D. A Short Introduction to the Lindblad Master Equation. AIP Adv 2020, 10 (2), 025106.
- (53) Redfield, A. G. The Theory of Relaxation Processes. *Adv. Magn. Reson.* **1965**, *1*, 1.
- (54) Nitzan, A.The Quantum Mechanical Density Operator And Its Time Evolution: Quantum Dynamics Using The Quantum Liouville Equation. In Chemical Dynamics In Condensed Phases: relaxation, Transfer And Reactions In Condensed Molecular Systems; Oxford University Press, 2006.
- (55) Brenes, M.; Mendoza-Arenas, J. J.; Purkayastha, A.; Mitchison, M. T.; Clark, S. R.; Goold, J. Tensor-Network Method to Simulate Strongly Interacting Quantum Thermal Machines. *Phys. Rev. X* **2020**, *10* (3), 031040.
- (56) Huang, Z.; Lin, L.; Park, G.; Zhu, Y. Unified Analysis of Non-Markovian Open Quantum Systems in Gaussian Environment Using Superoperator Formalism. *arXiv* **2024**, DOI: 10.48550/arXiv.2411.08741.
- (57) Makri, N.; Makarov, D. E. Tensor Propagator for Iterative Quantum Time Evolution of Reduced Density Matrices. I. Theory. *J. Chem. Phys.* **1995**, *102* (11), 4600–4610.
- (58) Makri, N.; Makarov, D. E. Tensor Propagator for Iterative Quantum Time Evolution of Reduced Density Matrices. II. Numerical Methodology. *J. Chem. Phys.* **1995**, *102* (11), 4611–4618.
- (59) Jin, J.; Zheng, X.; Yan, Y. Exact Dynamics of Dissipative Electronic Systems and Quantum Transport: Hierarchical Equations of Motion Approach. J. Chem. Phys. 2008, 128 (23), 234703.
- (60) Shi, Q.; Chen, L.; Nan, G.; Xu, R.-X.; Yan, Y. Efficient Hierarchical Liouville Space Propagator to Quantum Dissipative Dynamics. *J. Chem. Phys.* **2009**, *130* (8), 084105.
- (61) Strümpfer, J.; Schulten, K. Light Harvesting Complex II B850 Excitation Dynamics. J. Chem. Phys. 2009, 131 (22), 225101.
- (62) Shi, Q.; Chen, L.; Nan, G.; Xu, R.; Yan, Y. Electron Transfer Dynamics: Zusman Equation versus Exact Theory. *J. Chem. Phys.* **2009**, *130* (16), 164518.
- (63) Shi, Q.; Xu, Y.; Yan, Y.; Xu, M. Efficient Propagation of the Hierarchical Equations of Motion Using the Matrix Product State Method. *J. Chem. Phys.* **2018**, *148* (17), 174102.

- (64) Xu, R.-X.; Yan, Y. Dynamics of Quantum Dissipation Systems Interacting with Bosonic Canonical Bath: Hierarchical Equations of Motion Approach. *Phys. Rev. E* **2007**, *75* (3), 031107.
- (65) Orús, R. Tensor Networks for Complex Quantum Systems. Nat. Rev. Phys. 2019, 1 (9), 538-550.
- (66) Schollwöck, U. The Density-Matrix Renormalization Group in the Age of Matrix Product States. *Ann. Phys.* **2011**, 326 (1), 96–192.
- (67) Ke, Y.; Borrelli, R.; Thoss, M. Hierarchical Equations of Motion Approach to Hybrid Fermionic and Bosonic Environments: Matrix Product State Formulation in Twin Space. *J. Chem. Phys.* **2022**, *156* (19), 194102.
- (68) Ke, Y. Tree Tensor Network State Approach for Solving Hierarchical Equations of Motion. *J. Chem. Phys.* **2023**, *158* (21), 211102.
- (69) Gao, X.; Ren, J.; Eisfeld, A.; Shuai, Z. Non-Markovian Stochastic Schrödinger Equation: Matrix-Product-State Approach to the Hierarchy of Pure States. *Phys. Rev. A* **2022**, *105* (3), L030202.
- (70) Zhou, L.; Gao, X.; Shuai, Z. A Stochastic Schrödinger Equation and Matrix Product State Approach to Carrier Transport in Organic Semiconductors with Nonlocal Electron—Phonon Interaction. *J. Chem. Phys.* **2024**, *161* (8), 084118.
- (71) Takahashi, H.; Borrelli, R. Tensor-Train Format Hierarchical Equations of Motion Formalism: Charge Transfer in Organic Semiconductors via Dissipative Holstein Models. *J. Chem. Theory Comput.* **2024**, 20 (16), 7052–7064.
- (72) Li, W.; Ren, J.; Shuai, Z. Numerical Assessment for Accuracy and GPU Acceleration of TD-DMRG Time Evolution Schemes. *J. Chem. Phys.* **2020**, 152 (2), 024127.
- (73) Ren, J.; Li, W.; Jiang, T.; Shuai, Z. A General Automatic Method for Optimal Construction of Matrix Product Operators Using Bipartite Graph Theory. *J. Chem. Phys.* **2020**, *153* (8), 084118.
- (74) Fischer, E. W.; Saalfrank, P. A Thermofield-Based Multilayer Multiconfigurational Time-Dependent Hartree Approach to Non-Adiabatic Quantum Dynamics at Finite Temperature. *J. Chem. Phys.* **2021**, *155* (13), 134109.
- (75) Takahashi, Y.; Umezawa, H. THERMO FIELD DYNAMICS. *Int. J. Mod. Phys. B* **1996**, *10* (13n14), 1755–1805.
- (76) Borrelli, R.; Gelin, M. F. Simulation of Quantum Dynamics of Excitonic Systems at Finite Temperature: An Efficient Method Based on Thermo Field Dynamics. *Sci. Rep.* **2017**, *7* (1), 9127.
- (77) Leggett, A. J.; Chakravarty, S.; Dorsey, A. T.; Fisher, M. P. A.; Garg, A.; Zwerger, W. Dynamics of the Dissipative Two-State System. *Rev. Mod. Phys.* **1987**, *59* (1), 1–85.
- (78) Ishizaki, A.; Fleming, G. R. Theoretical Examination of Quantum Coherence in a Photosynthetic System at Physiological Temperature. *Proc. Natl. Acad. Sci. U. S. A.* **2009**, *106* (41), 17255–17260
- (79) Ye, L.; Wang, X.; Hou, D.; Xu, R.-X.; Zheng, X.; Yan, Y. HEOM-QUICK: A Program for Accurate, Efficient, and Universal Characterization of Strongly Correlated Quantum Impurity Systems. Wiley Interdiscip. Rev.: Comput. Mol. Sci. 2016, 6 (6), 608–638.
- (80) Borrelli, R. Density Matrix Dynamics in Twin-Formulation: An Efficient Methodology Based on Tensor-Train Representation of Reduced Equations of Motion. *J. Chem. Phys.* **2019**, *150* (23), 234102.
- (81) Chan, G. K.-L.; Keselman, A.; Nakatani, N.; Li, Z.; White, S. R. Matrix Product Operators, Matrix Product States, and Ab Initio Density Matrix Renormalization Group Algorithms. *J. Chem. Phys.* **2016**, *145* (1), 014102.
- (82) Paeckel, S.; Köhler, T.; Swoboda, A.; Manmana, S. R.; Schollwöck, U.; Hubig, C. Time-Evolution Methods for Matrix-Product States. *Ann. Phys.* **2019**, *411*, 167998.
- (83) José García-Ripoll, J. Time Evolution of Matrix Product States. *New J. Phys.* **2006**, 8 (12), 305.
- (84) Haegeman, J.; Lubich, C.; Oseledets, I.; Vandereycken, B.; Verstraete, F. Unifying Time Evolution and Optimization with Matrix Product States. *Phys. Rev. B* **2016**, *94* (16), 165116.
- (85) Haegeman, J.; Cirac, J. I.; Osborne, T. J.; Pižorn, I.; Verschelde, H.; Verstraete, F. Time-Dependent Variational Principle for Quantum Lattices. *Phys. Rev. Lett.* **2011**, *107* (7), 070601.

- (86) Ho, W. W.; Choi, S.; Pichler, H.; Lukin, M. D. Periodic Orbits, Entanglement, and Quantum Many-Body Scars in Constrained Models: Matrix Product State Approach. *Phys. Rev. Lett.* **2019**, *122* (4), 040603.
- (87) Xie, X.; Liu, Y.; Yao, Y.; Schollwöck, U.; Liu, C.; Ma, H. Time-Dependent Density Matrix Renormalization Group Quantum Dynamics for Realistic Chemical Systems. *J. Chem. Phys.* **2019**, *151* (22), 224101.
- (88) Olivares-Amaya, R.; Hu, W.; Nakatani, N.; Sharma, S.; Yang, J.; Chan, G. K.-L. The Ab-Initio Density Matrix Renormalization Group in Practice. *J. Chem. Phys.* **2015**, *142* (3), 034102.
- (89) Moritz, G.; Hess, B. A.; Reiher, M. Convergence Behavior of the Density-Matrix Renormalization Group Algorithm for Optimized Orbital Orderings. *J. Chem. Phys.* **2005**, *122* (2), 024107.
- (90) Wang, H.; Thoss, M. Theoretical Study of Ultrafast Photoinduced Electron Transfer Processes in Mixed-Valence Systems. *J. Phys. Chem. A* **2003**, *107* (13), 2126–2136.
- (91) Žitko, R.; Pruschke, T. Energy Resolution and Discretization Artifacts in the Numerical Renormalization Group. *Phys. Rev. B* **2009**, 79 (8), 085106.
- (92) Wang, D.; Chen, L.; Zheng, R.; Wang, L.; Shi, Q. Communications: A Nonperturbative Quantum Master Equation Approach to Charge Carrier Transport in Organic Molecular Crystals. *J. Chem. Phys.* **2010**, *1*32 (8), 081101.
- (93) Gelin, M. F.; Velardo, A.; Borrelli, R. Efficient Quantum Dynamics Simulations of Complex Molecular Systems: A Unified Treatment of Dynamic and Static Disorder. *J. Chem. Phys.* **2021**, *155* (13), 134102.

